

E-PCN: Jet Tagging with Explainable Particle Chebyshev Networks Using Kinematic Features

Md Raqibul Islam^{a,†} Adrita Khan^{a,†} Mir Sazzat Hossain^{a,*} Choudhury Ben Yamin Siddiqui^a Md. Zakir Hossan^a Tanjib Khan^c M. Arshad Momen^{a,b} Amin Ahsan Ali^a AKM Mahbubur Rahman^a

^a Center for Computational & Data Sciences, Independent University, Bangladesh, Dhaka-1229, Bangladesh

^b Department of Physical Sciences, Independent University, Bangladesh, Dhaka-1229, Bangladesh

^c Department of Theoretical Physics, University of Dhaka, Dhaka-1000, Bangladesh

E-mail: sazzat@iub.edu.bd

ABSTRACT: The identification and classification of collimated particle sprays, or jets, are essential for interpreting data from high-energy collider experiments. While deep learning has improved jet classification, it often lacks interpretability. We introduce the Explainable Particle Chebyshev Network (E-PCN), a graph neural network extending the Particle Chebyshev Network (PCN). E-PCN integrates kinematic variables into jet classification by constructing four graph representations per jet, each weighted by a distinct variable: angular separation (Δ), transverse momentum (k_T), momentum fraction (z), and invariant mass squared (m^2). We use the concept of Gradient-weighted Class Activation Mapping (Grad-CAM) to determine which kinematic variables dominate classification outcomes. Analysis reveals that angular separation and transverse momentum collectively account for approximately 76% of classification decisions (40.72% and 35.67%, respectively), with momentum fraction and invariant mass contributing the remaining 24%. Evaluated on the JetClass dataset with 10 signal classes, E-PCN achieves a macro-accuracy of 94.67%, macro-AUC of 96.78%, and macro-AUPR of 86.79%, representing improvements of 2.36%, 4.13%, and 24.88% respectively over the baseline PCN implementation, while demonstrating physically interpretable feature learning.

KEYWORDS: Jets and Jet Substructure, Top Quark, Bottom Quarks

† These authors contributed equally to this work.

* Corresponding authors

Code: <https://github.com/ccdsiub/E-PCN>

Contents

1	Introduction	2
2	Related Work	3
3	Methodology	4
3.1	Dataset	5
3.2	Graph Representation of Jets	5
3.3	Edge-Weighted Multi-Graph	6
3.4	Neural Network Architecture	6
3.5	Training Configuration	8
3.6	Kinematic Variable Importance	8
4	Results	9
4.1	Classification Accuracy	9
4.2	Area Under the Curve (AUC)	9
4.3	Area Under Precision-Recall Curve (AUPR)	10
4.4	Comparison to State-of-the-Art Models	10
4.5	Explainability Analysis	11
5	Ablation Studies	12
5.1	Impact of Individual kinematic variables	13
5.2	Impact Hyperparameter Tuning on the Model	13
6	Discussion	14
7	Conclusion	16
A	Computational Resources	20
B	Pseudocode	20
C	Feature name and Description	24

1 Introduction

The High-Luminosity Large Hadron Collider (HL-LHC) upgrade will increase the integrated luminosity by approximately one order of magnitude compared to the baseline LHC [1, 2], introducing data processing challenges. Machine learning (ML) is one approach for extracting physics insights from such high volume data. A key application is jet tagging, the process of identifying the particle responsible for initiating a jet [3, 4].

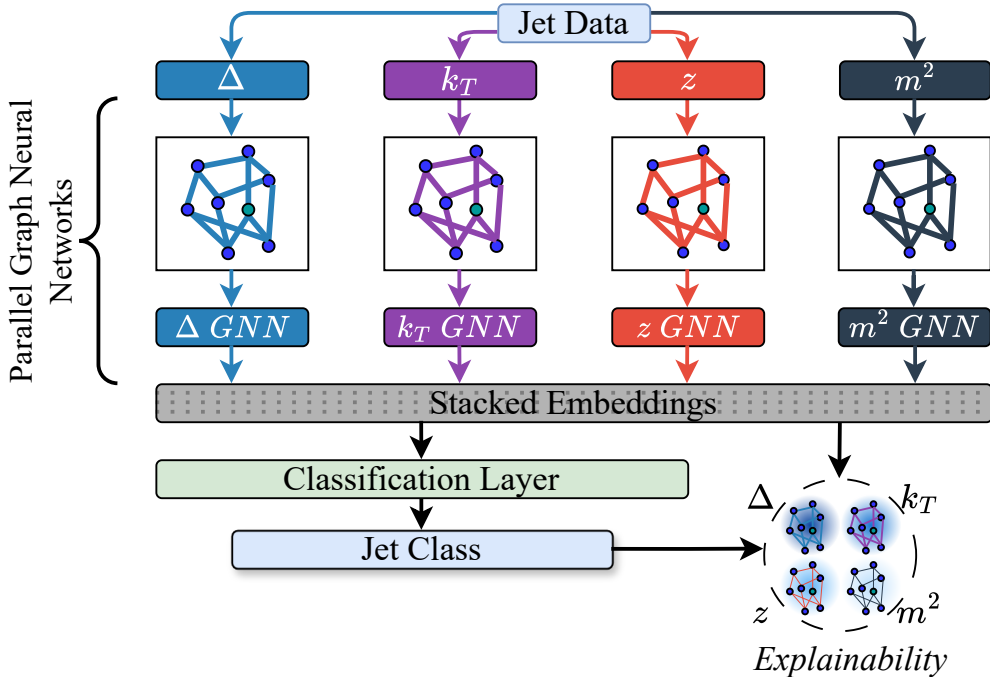


Figure 1. E-PCN, with integrated explainability analysis. Data is processed through four parallel GNNs, each weighted by a distinct kinematic variables: angular separation (Δ), transverse momentum (k_T), momentum fraction (z), and invariant mass squared (m^2) of each pair of the particles involved. The embeddings from all GNNs are stacked and classified into jet classes. A detailed architectural diagram is provided in Figure 2, and the model is formally described in Section 3.4.

Many ML approaches address jet tagging [5–8], and graph neural networks (GNNs) [9–11] are one of them. GNNs treat jets as graphs with particles as nodes and inter-particle relationships as edges, accommodating the permutation-invariant and variable-length nature of jet constituent data. Within GNN architectures, Particle Chebyshev Network (PCN) [12] represents a contribution to graph-based jet tagging through its use of Chebyshev graph convolutions [13–15] to process jet constituents. Unlike spatial GNN methods that operate directly on graph structure, spectral approaches define convolutions in the Fourier domain of the graph Laplacian [16, 17], with Chebyshev polynomials [18] providing a computationally tractable approximation [19]. The PCN architecture achieves strong performance on benchmark datasets by combining Chebyshev graph convolutions with edge convolutions

[20]. However, understanding how ML models make classification decisions has become increasingly important. When models inform new discoveries, the ability to interpret and validate model behavior is critical for ensuring that learned features correspond to physical phenomena rather than detector artifacts or spurious correlations. Spectral methods like PCN, while powerful, typically obscure the explicit relationship between graph structure and learned representations, hindering physical interpretation [21].

We address this limitation by introducing the **Explainable Particle Chebyshev Network (E-PCN)**, an extension of the PCN, that integrates four kinematic variables between each pair of the particles involving quantities namely Δ (angular separation), k_T (transverse momentum), z (momentum fraction), and m^2 (invariant mass squared) directly into the classification process. Figure 1 illustrates E-PCN, which processes jet data through four parallel Graph Neural Networks (GNNs), each weighted by one of these kinematic variables, with embeddings combined and classified into jet classes. E-PCN constructs a representation that incorporates these kinematic variables as edge weights while processing node-level features through Chebyshev graph convolutions. Throughout this paper, we use the terms “**interaction features**” and “**kinematic variables**” interchangeably.

The remainder of this paper is organized as follows. Section 2 reviews related work on jet tagging. Section 3 presents the E-PCN framework, including dataset description, graph representation, network architecture, and training configuration. Section 4 reports results, including classification metrics, model comparisons, and Grad-CAM [22] analysis. Section 5 presents ablation studies, followed by the discussion in Section 6 and the conclusion in Section 7.

2 Related Work

Convolutional neural networks proved competitive for jet tagging starting in 2015, when applied to calorimeter energy deposits and matching the performance of conventional approaches [23]. While learned representations replaced handcrafted features, pixelization of detector geometry caused information loss and fixed grids struggled with variable particle multiplicities; recognizing that jets are inherently sparse and variable in size, sequential models were introduced to address these limitations. Recursive Neural Networks modeled the hierarchical structure of jet clustering [24], while P-CNN represented jets as fixed-length sequences of particles sorted by transverse momentum [25]. P-CNN used particle-level kinematic information with 1D convolutions, demonstrating the feasibility of particle-based approaches. However, sorting imposed artificial ordering on an unordered system. To address this limitation, permutation-invariant architectures were developed that treat jets as unordered sets. Energy Flow Networks incorporated infrared and collinear (IRC) safety through the Deep Sets framework [26], providing constraints on learned features grounded in particle physics. Particle Flow Networks (PFN) used full particle kinematic information while relaxing IRC safety constraints [26].

Building on set-based representations, jets were also represented as point clouds in kinematic space, enabling Graph Neural Networks to capture pairwise and many-body interactions. ParticleNet employed dynamic graph convolutions (EdgeConv) that update

neighbor relations in latent space [5]. JEDI-net modeled explicit pairwise particle interactions [27], and LundNet incorporated geometric priors from the Lund plane representation [28]. More recent architectures enforce exact physical symmetries. The Particle Transformer (ParT) adapted attention mechanisms with learned pairwise interaction biases and outperformed GNN baselines [8]. LorentzNet and PELICAN demonstrated that Lorentz-equivariant architectures achieve state-of-the-art performance with fewer parameters [9, 29]. While these approaches achieve high classification accuracy, their computational demands limit real-time deployment at the LHC. The High-Luminosity LHC upgrade will increase collision rates by an order of magnitude [1, 2], requiring taggers that operate within microsecond-scale latency constraints. Recent work has focused on reducing computational cost while maintaining performance. The Particle Chebyshev Network (PCN) approximates graph convolutions using Chebyshev polynomials, avoiding expensive dynamic graph construction while retaining competitive accuracy [12]. JEDI-linear achieves sub-microsecond latency [30], and SAL-T linearizes transformer attention mechanisms [31].

The kinematic variables used in this work are motivated by the Lund jet plane [32], which provides a two-dimensional representation of jet substructure by mapping iterative declustering onto the $(\ln k_T, \ln \Delta)$ plane. Each splitting $i \rightarrow j+k$ in the Cambridge/Aachen clustering history [33, 34] is described by four kinematic variables derived from particle four-momenta $p = (E, p_x, p_y, p_z)$:

$$\Delta_{ab} = \sqrt{(y_a - y_b)^2 + (\phi_a - \phi_b)^2} \quad (2.1)$$

$$k_{T,ab} = \min(p_{T,a}, p_{T,b}) \cdot \Delta_{ab} \quad (2.2)$$

$$z_{ab} = \frac{\min(p_{T,a}, p_{T,b})}{p_{T,a} + p_{T,b}} \quad (2.3)$$

$$m_{ab}^2 = (E_a + E_b)^2 - \|\vec{p}_a + \vec{p}_b\|^2 \quad (2.4)$$

where y_i is rapidity, ϕ_i is azimuthal angle, $p_{T,i} = \sqrt{p_{x,i}^2 + p_{y,i}^2}$ is transverse momentum, and $\vec{p}_i = (p_{x,i}, p_{y,i}, p_{z,i})$ is the momentum three-vector. The invariant mass m_{ab}^2 corresponds to the Mandelstam variable s [35]. These variables exhibit long-tailed distributions spanning multiple orders of magnitude. Following Dreyer & Qu [28], we use their logarithmic forms $(\ln \Delta, \ln k_T, \ln z, \ln m^2)$ as interaction features.

In our paper, we extend the PCN framework by incorporating kinematic variables through a multi-graph architecture, E-PCN. The model constructs four parallel graph representations weighted by Δ , k_T , z , and m^2 , enabling specialized feature extraction for each quantity.

3 Methodology

This section describes E-PCN, our proposed approach for jet classification. We begin by introducing the dataset in Section 3.1, then explain how jets are represented as graphs in Section 3.2. We describe the physics-motivated edge-weighted multi-graph architecture

in Section 3.3, present the neural network architecture in Section 3.4, and conclude with training configuration in Section 3.5.

3.1 Dataset

We conducted our experiments on the **JetClass** dataset [8, 36], a large-scale benchmark designed to advance deep learning research in jet physics. **JetClass** comprises 100 million jets for training, 5 million for validation, and 20 million for testing, distributed across **10 distinct jet classes**. These classes represent different particle production and decay channels, divided into two main categories: signal jets originating from heavy particles (top quarks and Higgs, W, Z bosons) and background jets produced by light quarks and gluons. The 10 jet classes include Higgs boson decays ($H \rightarrow b\bar{b}$, $H \rightarrow c\bar{c}$, $H \rightarrow gg$, $H \rightarrow 4q$, $H \rightarrow \ell\nu qq'$), top quark decays ($t \rightarrow bqq'$, $t \rightarrow b\ell\nu$), electroweak boson decays ($W \rightarrow qq'$, $Z \rightarrow q\bar{q}$), and background jets from light quarks and gluons (q/g). Table 1 presents the complete taxonomy.

Class	Decay Process	Description
1	$H \rightarrow b\bar{b}$	Higgs boson decays to bottom quark-antiquark pair
2	$H \rightarrow c\bar{c}$	Higgs boson decays to charm quark-antiquark pair
3	$H \rightarrow gg$	Higgs boson decays to two gluons
4	$H \rightarrow 4q$	Higgs boson decays to four quarks
5	$H \rightarrow \ell\nu qq'$	Higgs boson decays to lepton, neutrino, and two quarks
6	$t \rightarrow bqq'$	Top quark decays to bottom quark and two other quarks
7	$t \rightarrow b\ell\nu$	Top quark decays to bottom quark, lepton, and neutrino
8	$W \rightarrow qq'$	W boson decays to two quarks
9	$Z \rightarrow q\bar{q}$	Z boson decays to quark-antiquark pair
10	$Z \rightarrow \ell^+\ell^-$	Z boson decays to lepton-antilepton pair

Table 1. Signal classes in the **JetClass** dataset representing various particle production and decay channels.

For computational efficiency while preserving class balance, we employ a subset of 1 million training jets (100,000 per class), the full 5 million validation jets (500,000 per class), and the full 20 million test jets (2 million per class). Table 2 details the dataset partitioning.

Subset	Total Jets	Per Class
Training	1,000,000	100,000
Validation	5,000,000	500,000
Test	20,000,000	2,000,000

Table 2. Dataset split used for model development and evaluation.

3.2 Graph Representation of Jets

We represent each jet as a graph $G = (V, E)$ where particles are nodes V and connections among nearby particles form edges E . For each particle, we connect it to its k=3 near-

est neighbors based on angular separation in (η, ϕ) space, where η is pseudorapidity and ϕ is azimuthal angle. This choice of $k = 3$ neighbors balances capturing local structure while avoiding excessive noise from distant particles. The nearest-neighbor search uses a KD-tree for computational efficiency (algorithm 1). Each particle node carries 16 features: momentum components (p_x, p_y, p_z) , energy E , transverse momentum p_T , angular coordinates (η, ϕ) , impact parameters (measuring displacement from the collision point), and one-hot encoded flags indicating particle type (charged hadron, neutral hadron, photon, electron, or muon). These features are concatenated into a single 16-dimensional vector for each particle. Table 12 lists all input features.

3.3 Edge-Weighted Multi-Graph

A key contribution of E-PCN is incorporating kinematic variables through four quantities computed for each pair of connected particles. These quantities capture different aspects of how energy and momentum are shared between particles, which is informative for distinguishing different jet types. Angular separation (Δ), Transverse momentum (k_T), Momentum fraction (z) and Invariant mass squared (m^2) are computed according to the equations (2.1)–(2.4). We take the logarithm and use $(\ln \Delta, \ln k_T, \ln z, \ln m^2)$ as the kinematic variables for each particle pair, since these quantities vary over many orders of magnitude and their log-transformed versions exhibit more well-behaved distributions for training (algorithm 2). We create four separate graph representations of the same jet using these kinematic variables. All four graphs share identical node features (the 16 particle properties) and the same connectivity (edges to nearest neighbors), but each graph uses a different quantity as its edge weight: G_Δ edges weighted by $\ln \Delta$, G_{k_T} edges weighted by $\ln k_T$, G_z edges weighted by $\ln z$ and G_{m^2} edges weighted by $\ln m^2$. This design allows the network to learn specialized representations for each type of particle relationship, rather than requiring a single network to balance all four aspects simultaneously (algorithm 3).

3.4 Neural Network Architecture

The E-PCN architecture processes the four graph representations in parallel through identical but independently parameterized networks, then combines their outputs for final classification. Figure 2 illustrates the complete pipeline.

Feature Extraction – Each of the four graphs passes through its own feature extractor consisting of five graph convolutional layers. We alternate between two complementary types of graph convolutions: **Chebyshev convolutions** (ChebConv), which operate on the graph structure using spectral methods and aggregate information from a node’s local neighborhood using polynomial filters of order 16, enabling each node to incorporate information from particles up to 16 hops away; and **edge convolutions** (EdgeConv), which focus on pairwise relationships between connected particles and learn features from the differences between neighboring nodes. The alternating pattern (ChebConv \rightarrow EdgeConv \rightarrow ChebConv \rightarrow EdgeConv \rightarrow ChebConv) allows the network to capture both local geometric structure and broader graph-level patterns. Each convolutional layer is followed by batch normalization and ReLU activation. The initial layer transforms the 16-dimensional input

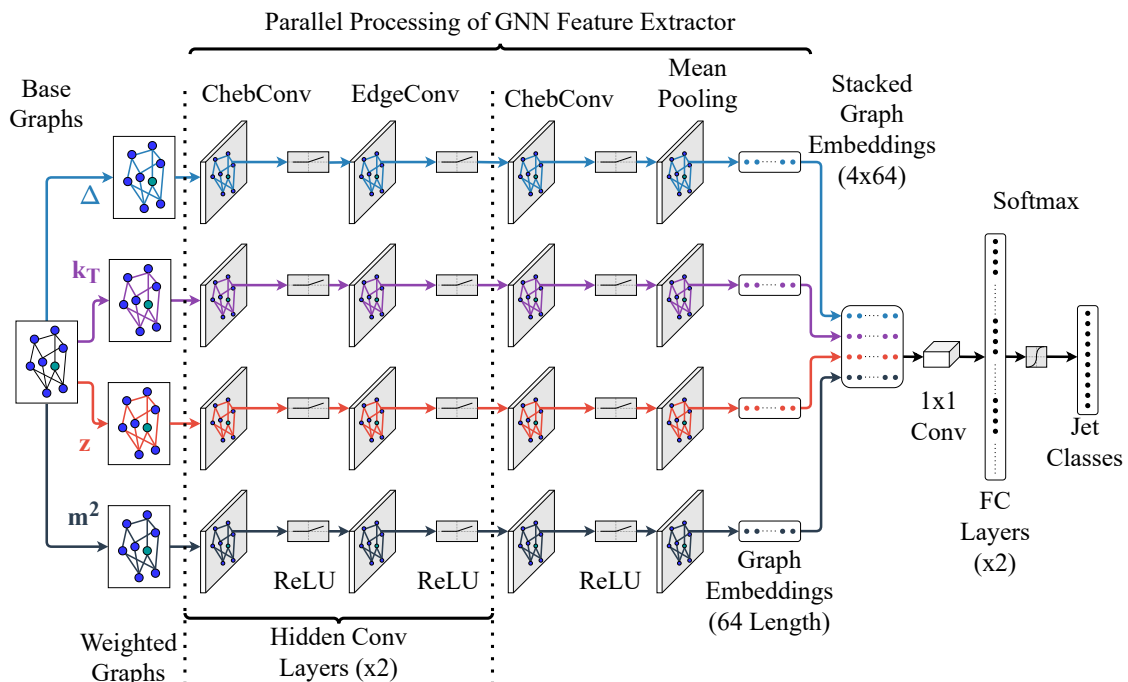


Figure 2. Architecture of the proposed E-PCN model showing four parallel graph processing branches (G_Δ , G_{k_T} , G_Z , G_{m^2}) with hybrid convolutional layers. Each branch processes a distinct graph representation through alternating Chebyshev graph convolutions (ChebConv) and edge convolutions (EdgeConv), generating 64-dimensional embeddings. The four embeddings are combined via 1D convolution and passed through fully connected layers for final classification into 10 jet categories.

features to 64-dimensional hidden representations, maintained through subsequent layers (algorithm 4).

Graph-Level Pooling – After the final convolutional layer, we aggregate all particle-level features into a single 64-dimensional vector representing the entire jet using mean pooling: averaging features across all particles. This produces four embedding vectors per jet, one from each graph branch.

Multi-Graph Combination – The four 64-dimensional vectors are stacked into a 4×64 matrix. We apply a 1D convolution with kernel size 1 across the four graph channels, which learns how to weight and combine information from the different kinematic representations.

Classification – The combined representation is flattened to a 256-dimensional vector and passed through two fully connected layers with dropout rate 0.1 for regularization. The first layer reduces dimensionality to 64, and the second produces 10 outputs corresponding to the 10 jet classes. A softmax function converts these outputs to class probabilities (algorithm 5).

3.5 Training Configuration

Hyperparameters – Table 3 details the hyperparameters used for E-PCN training and architecture.

Optimization		Architecture	
Optimizer	AdamW	Hidden Dim.	64
Learning Rate	10^{-3}	Graph Branches	4
Batch Size	256	ChebConv Order	16
Max Epochs	500	k -NN	3
Early Stop	10 epochs	Conv. Layers	5
Conv. Threshold	10^{-4}	Output Classes	10
Regularization			
Dropout Rate		0.1	

Table 3. Hyperparameters for E-PCN training and architecture.

Training Procedure – Jets are loaded in batches of 256 with random shuffling at each epoch. For each jet, the four graphs (G_{Δ} , G_{k_T} , G_z , G_{m^2}) are constructed on-the-fly using k -NN connectivity based on angular distance in (η, ϕ) space. Each graph is independently processed through its respective feature extractor, yielding four 64-dimensional embeddings that are subsequently combined via 1D convolution. Cross-entropy loss is minimized, and network parameters are updated via the AdamW optimizer with learning rate 10^{-3} . Training employs early stopping: termination occurs when validation loss shows no improvement exceeding 10^{-4} over 10 consecutive epochs.

3.6 Kinematic Variable Importance

We adapt Gradient-weighted Class Activation Mapping (Grad-CAM) [22] (illustrated in Figure 3), a technique originally developed for interpreting convolutional neural networks, to our multi-graph architecture. Our model processes four distinct graph types through dedicated feature extractors, each producing 64-dimensional embeddings. For each graph type, we compute the gradient of the predicted class score with respect to its corresponding embedding to measure variable importance. The importance of each graph type is calculated as the product of the gradient magnitude and the embedding magnitude, then globally averaged across the 64 embedding dimensions, yielding a scalar importance score for each graph type. Understanding which kinematic variables drive the model’s decisions is essential for validating that the network learns physically meaningful features and for identifying potential biases in the training data. We compute importance scores independently for each test sample and each jet type. To characterize global variable importance, we average these scores across all test samples. Separately, we compute class-specific importance by averaging only over samples of a particular jet type, revealing which kinematic variables are most discriminative for distinguishing each jet class. To facilitate comparison, we normalize the four importance scores to percentages that sum to 100%, ensuring that

the relative contribution of each graph type is interpretable. The detailed procedure is outlined in Algorithm 6.

4 Results

This section presents evaluation of E-PCN on the `JetClass` dataset. We first report classification accuracy across all ten signal classes in Section 4.1, followed by an analysis of Area Under the Curve (AUC) metrics in Section 4.2 and Area Under the Precision-Recall Curve (AUPR) in Section 4.3. We then compare E-PCN with existing state-of-the-art models in Section 4.4, and finally provide an explainability analysis using Gradient-weighted Class Activation Mapping (Grad-CAM) in Section 4.5.

**PCN* denotes our reimplementation of the baseline Particle Chebyshev Network trained on 1M jets (100K per class) from the `JetClass` dataset.

4.1 Classification Accuracy

Table 4 presents the classification accuracies for all ten signal classes in the `JetClass` dataset.

	Macro-Acc	$H \rightarrow b\bar{b}$ Acc	$H \rightarrow c\bar{c}$ Acc	$H \rightarrow gg$ Acc	$H \rightarrow 4q$ Acc	$H \rightarrow lvqq'$ Acc	$t \rightarrow bqq'$ Acc	$t \rightarrow blv$ Acc	$W \rightarrow qq'$ Acc	$Z \rightarrow q\bar{q}$ Acc	$Z \rightarrow \ell^+\ell^-$ Acc
PCN*	0.9249	0.9045	0.8992	0.8986	0.9089	0.9635	0.9483	0.9773	0.9182	0.9331	0.8979
E-PCN (ours)	0.9467	0.9564	0.9300	0.9313	0.9325	0.9815	0.9677	0.9878	0.9248	0.9444	0.9109
Improvement (%)	+2.36%	+5.74%	+3.43%	+3.64%	+2.60%	+1.87%	+2.05%	+1.07%	+0.72%	+1.21%	+1.45%

Table 4. Classification accuracy comparison on the 10 signal classes in the `JetClass` dataset. Macro-Acc represents the macro-averaged accuracy across all classes.

E-PCN achieves a macro-averaged accuracy of 0.9467, representing a 2.36% improvement over PCN* (0.9249). The model outperforms the baseline across all signal classes. The $H \rightarrow b\bar{b}$ class shows the largest gain of 5.74% (0.9564 vs. 0.9045), followed by $H \rightarrow gg$ with 3.64% (0.9313 vs. 0.8986) and $H \rightarrow c\bar{c}$ with 3.43% (0.9300 vs. 0.8992). The $H \rightarrow 4q$ class improves by 2.60% (0.9325 vs. 0.9089). Among top quark decays, $t \rightarrow bqq'$ achieves 0.9677 (+2.05%) and $t \rightarrow blv$ reaches 0.9878 (+1.07%). The $H \rightarrow lvqq'$ class attains 0.9815 (+1.87%). Vector boson decays show improvements of 0.72% for $W \rightarrow qq'$ (0.9248), 1.21% for $Z \rightarrow q\bar{q}$ (0.9444), and 1.45% for $Z \rightarrow \ell^+\ell^-$ (0.9109).

4.2 Area Under the Curve (AUC)

Table 5 compares the AUC performance of the models. E-PCN achieves a macro-averaged AUC of 0.9678, a 4.13% improvement over the PCN* baseline (0.9294).

The largest performance gains occur in the heavy flavor quark channels: $H \rightarrow b\bar{b}$ improves by 11.16% (0.8781 to 0.9761) and $H \rightarrow c\bar{c}$ by 7.58% (0.8633 to 0.9287). Other Higgs decay channels show consistent increases, with $H \rightarrow gg$ up 3.38% and $H \rightarrow 4q$ up 2.22%. In the top quark sector, $t \rightarrow bqq'$ and $t \rightarrow blv$ reach AUCs of 0.9872 (+1.38%) and 0.9975 (+0.46%), respectively. Vector boson decays also improve, with $W \rightarrow qq'$ rising

	Macro-AUC	$H \rightarrow b\bar{b}$ AUC	$H \rightarrow c\bar{c}$ AUC	$H \rightarrow gg$ AUC	$H \rightarrow 4q$ AUC	$H \rightarrow lvqq'$ AUC	$t \rightarrow bqq'$ AUC	$t \rightarrow blv$ AUC	$W \rightarrow qq'$ AUC	$Z \rightarrow q\bar{q}$ AUC	$Z \rightarrow \ell^+\ell^-$ AUC
PCN*	0.9294	0.8781	0.8633	0.9190	0.9362	0.9825	0.9738	0.9929	0.9313	0.9316	0.8857
E-PCN (ours)	0.9678	0.9761	0.9287	0.9501	0.9570	0.9941	0.9872	0.9975	0.9507	0.9531	0.9199
Improvement (%)	+4.13%	+11.16%	+7.58%	+3.38%	+2.22%	+1.18%	+1.38%	+0.46%	+2.08%	+2.31%	+3.86%

Table 5. Area Under the ROC Curve (AUC) comparison on the 10 signal classes in the `JetClass` dataset. Macro-AUC represents the macro-averaged AUC across all classes.

2.08% to 0.9507 and $Z \rightarrow q\bar{q}$ rising 2.31% to 0.9531. The leptonic Z decay ($Z \rightarrow \ell^+\ell^-$) improves by 3.86%.

4.3 Area Under Precision-Recall Curve (AUPR)

Table 6 details the AUPR performance, a metric for imbalanced datasets. E-PCN achieves a macro-averaged AUPR of 0.8241, a 24.88% improvement over the PCN* baseline (0.6599).

	Macro-AUPR	$H \rightarrow b\bar{b}$ AUPR	$H \rightarrow c\bar{c}$ AUPR	$H \rightarrow gg$ AUPR	$H \rightarrow 4q$ AUPR	$H \rightarrow lvqq'$ AUPR	$t \rightarrow bqq'$ AUPR	$t \rightarrow blv$ AUPR	$W \rightarrow qq'$ AUPR	$Z \rightarrow q\bar{q}$ AUPR	$Z \rightarrow \ell^+\ell^-$ AUPR
PCN*	0.6599	0.4738	0.4577	0.5741	0.6431	0.8999	0.8043	0.9532	0.6024	0.7513	0.4389
E-PCN (ours)	0.8241	0.8601	0.6936	0.7242	0.7266	0.9658	0.9085	0.9837	0.6694	0.8047	0.5679
Improvement (%)	+24.88%	+81.53%	+51.54%	+26.15%	+12.98%	+7.32%	+12.96%	+3.20%	+11.12%	+7.11%	+29.39%

Table 6. Area Under the Precision-Recall Curve (AUPR) comparison on the 10 signal classes in the `JetClass` dataset. Macro-AUPR represents the macro-averaged AUPR across all classes.

Higgs boson decay channels show the most significant gains. The $H \rightarrow b\bar{b}$ class improves by 81.53% (0.4738 to 0.8601), followed by $H \rightarrow c\bar{c}$ with 51.54% (0.4577 to 0.6936) and $H \rightarrow gg$ with 26.15% (0.5741 to 0.7242). The $H \rightarrow 4q$ channel improves by 12.98% to 0.7266. In the top quark sector, $t \rightarrow bqq'$ gains 12.96% (0.8043 to 0.9085), while $t \rightarrow blv$ reaches 0.9837 (+3.20%). The $H \rightarrow lvqq'$ channel achieves 0.9658 (+7.32%). Vector boson decays also exhibit strong improvements: $W \rightarrow qq'$ rises 11.12% to 0.6694, $Z \rightarrow q\bar{q}$ increases 7.11% to 0.8047, and $Z \rightarrow \ell^+\ell^-$ improves 29.39% to 0.5679. These results highlight E-PCN’s effectiveness in handling class imbalance and reducing false positives.

4.4 Comparison to State-of-the-Art Models

We compare E-PCN against five baseline models trained on the `JetClass` dataset: PCN* (our reimplementation), PFN [26], P-CNN [37], ParticleNet [5], and ParT [8]. Table 7 summarizes the performance metrics.

E-PCN sets a new benchmark for classification accuracy, achieving 0.9467 and outperforming the state-of-the-art ParT model (0.9312) by 1.55 percentage points. In terms of AUC, E-PCN demonstrates performance comparable to ParT (0.9678 vs. 0.9687), achieving near-perfect discrimination while offering superior accuracy. This trade-off is particularly beneficial for specific decay channels; for example, in the challenging $H \rightarrow b\bar{b}$ and $H \rightarrow c\bar{c}$ classes, E-PCN achieves AUC values of 0.9761 and 0.9287, respectively, surpassing ParT’s reported 0.9523 and 0.9089.

Model	Macro-Accuracy	Macro-AUC
PFN	0.8521 (+11.1%)	0.9103 (+6.3%)
P-CNN	0.8847 (+7.0%)	0.9312 (+3.9%)
ParticleNet	0.9015 (+5.0%)	0.9521 (+1.6%)
ParT	0.9312 (+1.7%)	0.9687 (-0.1%)
PCN* (baseline)	0.9249 (+2.4%)	0.9294 (+4.1%)
E-PCN (ours)	0.9467	0.9678

Table 7. Comparison of model performances on the `JetClass` dataset. Percentages in parentheses indicate the relative improvement of E-PCN over the corresponding method.

The model’s effectiveness stems from its multi-graph architecture, which processes kinematic variables (Δ , k_T , z , m^2) in parallel branches. This allows the network to capture complementary physical information—angular structure, momentum scales, energy sharing, and mass relationships—simultaneously. The convolution module dynamically weights these representations, leveraging explicit Lund plane features [32]. While this multi-branch design increases computational overhead compared to single-graph models, it provides gains in accuracy and precision-recall metrics. For latency-constrained applications such as LHC trigger systems, a weight-shared variant (see Section 5) offers a practical compromise, achieving 93.89% accuracy with significantly reduced parameter count.

4.5 Explainability Analysis

	$H \rightarrow b\bar{b}$	$H \rightarrow c\bar{c}$	$H \rightarrow gg$	$H \rightarrow 4q$	$H \rightarrow lvqq'$	$t \rightarrow bqq'$	$t \rightarrow blv$	$W \rightarrow qq'$	$Z \rightarrow q\bar{q}$	$Z \rightarrow \ell^+\ell^-$
Δ	38.27	39.98	38.37	39.13	45.05	38.32	43.98	39.19	42.61	38.96
k_T	35.59	36.40	40.24	38.93	31.72	38.74	30.60	37.44	33.61	37.74
z	12.49	13.93	13.30	14.26	14.55	12.22	14.77	15.36	15.54	14.42
m^2	13.64	09.68	08.09	07.68	08.68	10.72	10.66	08.01	08.24	08.88

Table 8. Feature importance analysis for jet classification using Gradient-weighted Class Activation Mapping (Grad-CAM). Values represent the relative contribution (%) of each kinematic variables, angular separation (Δ), transverse momentum (k_T), momentum fraction (z), and invariant mass (m^2), to the E-PCN classification decision for ten distinct jet classes. Highlighted values indicate which feature contributes most strongly to each classification task. The analysis reveals that *angular separation* and *transverse momentum* consistently provide the highest predictive values for most of the classes, together contributing for approximately 75% to the final predictions.

To understand which kinematic variables the network prioritizes when classifying jets, we apply an explainability analysis called Gradient-weighted Class Activation Mapping (Grad-CAM) [22]. This technique reveals how much each of the four graph representations, encoding Δ , k_T , z , and m^2 , contributes to the final classification decision. The method works by tracking how sensitive the network’s output is to each input feature: if changing a particular graph representation affects the prediction, that feature is deemed important. Table 8 presents a quantitative analysis of feature importance across the ten

jet classes using Gradient-weighted Class Activation Mapping (Grad-CAM). The analysis reveals distinct patterns in how the four kinematic variables contribute to classification decisions for different jet classification. Angular separation (Δ) demonstrates the highest contribution for most classes, ranging from 38.32% to 45.05%, with high importance for leptonic jet classes ($H \rightarrow \ell\nu qq'$ at 45.05% and $t \rightarrow b\ell\nu$ at 43.98%). Transverse momentum (k_T) shows complementary importance, contributing most strongly to gluon jets ($H \rightarrow gg$ at 40.24%) and hadronic top decays ($t \rightarrow bqq'$ at 38.74%). Together, these two dominant features (Δ and k_T) account for approximately 75% of the classification signal across all classes. The momentum fraction (z) maintains moderate importance across all classes (12.22% - 15.54%), while invariant mass squared (m^2) shows the lowest overall contribution (7.68% - 13.64%). Notably, m^2 exhibits higher relevance for heavy jets such as $H \rightarrow b\bar{b}$ (13.64%), consistent with theoretical expectations that invariant mass provides discrimination for heavy quark identification. These class-specific variations in feature importance demonstrate that E-PCN learns physically meaningful patterns of different jet formation mechanisms.

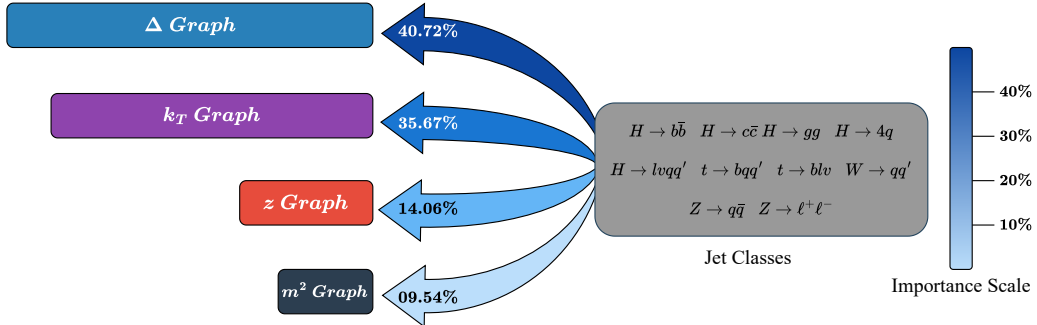


Figure 3. Grad-CAM explainability analysis quantifying feature importance in E-PCN classification. (a) Four graph representations undergo parallel processing through specialized GNN branches. (b) Feature attribution analysis shows that angular separation (Δ , 40.72%) and transverse momentum (k_T , 35.67%) dominate the classification decisions, while momentum fraction (z , 14.06%) and invariant mass (m^2 , 9.54%) provide complementary information (Algorithm 6).

Figure 3 presents the Grad-CAM results averaged over the test dataset. The analysis reveals a clear hierarchy: angular separation (Δ) accounts for 40.72% of the decision-making weight, followed by transverse momentum ordering (k_T) at 35.67%. Together, these two features drive over 76% of the classification signal. In contrast, momentum fraction (z) and invariant mass (m^2) contribute 14.06% and 9.54%, respectively.

5 Ablation Studies

To understand the individual contributions of each component in the E-PCN architecture, we conduct a systematic ablation study. We evaluate the impact of different kinematic variables and the multi-graph representation on overall classification performance.

Feature Combination	Δ	k_T	z	m^2	Acc.
Baseline (no features)	-	-	-	-	0.9249
Single feature					
Δ only	✓	-	-	-	0.9347
k_T only	-	✓	-	-	0.9304
z only	-	-	✓	-	0.9345
m^2 only	-	-	-	✓	0.9307
Two features					
Δ, k_T	✓	✓	-	-	0.9446
Δ, z	✓	-	✓	-	0.9423
Δ, m^2	✓	-	-	✓	0.9458
k_T, z	-	✓	✓	-	0.9435
k_T, m^2	-	✓	-	✓	0.9461
z, m^2	-	-	✓	✓	0.9335
Three features					
Δ, k_T, z	✓	✓	✓	-	0.9437
Δ, k_T, m^2	✓	✓	-	✓	0.9425
Δ, z, m^2	✓	-	✓	✓	0.9465
k_T, z, m^2	-	✓	✓	✓	0.9462
All four (E-PCN)	✓	✓	✓	✓	0.9467

Table 9. Ablation study on kinematic variables. Macro-averaged accuracy for different combinations of angular separation (Δ), transverse momentum (k_T), momentum fraction (z), and invariant mass (m^2). Checkmarks (✓) indicate included features; dashes (-) indicate exclusion. Baseline uses only 16-dimensional particle features. Best performance (94.67%) achieved with all four features in E-PCN.

5.1 Impact of Individual kinematic variables

Table 9 presents the macro-averaged accuracy for different subsets of the four kinematic variables. The baseline model—using only the original 16-dimensional particle features—achieves an accuracy of 92.49%. Among the single-feature configurations, Δ and z yield the strongest improvements (93.47% and 93.45%), while k_T and m^2 provide smaller but consistent gains (93.04% and 93.07%). For two-feature combinations, the highest accuracies are obtained when using the pair (k_T, m^2) (94.61%) or (Δ, m^2) (94.58%). In contrast, the combination of (z, m^2) performs comparatively poorly (93.35%), indicating partial redundancy between these two features. Most three-feature configurations exceed 94%, with (Δ, z, m^2) reaching the highest value of 94.65%. The full four-feature E-PCN model achieves the best overall performance at 94.67%, confirming that each kinematic variables contributes complementary information beyond the baseline representation.

5.2 Impact Hyperparameter Tuning on the Model

Table 10 presents an ablation study examining how different hyperparameters affect the E-PCN model’s performance on jet classification. We investigated four design choices: batch size, feature aggregation strategy, learning rate scheduling, and batch normalization. Our experiments reveal

Batch	Aggregation	LR Scheduler	BN	Macro Acc
2048	Horizontal	–	–	0.9332
1024	Horizontal	–	–	0.9381
512	Horizontal	–	–	0.9382
256	Horizontal	–	–	0.9387
2048	Vertical	–	–	0.9350
1024	Vertical	–	–	0.9381
512	Vertical	–	–	0.9387
256	Vertical	–	–	0.9399
256	Vertical	OneCycleLR	–	0.9421
256	Vertical	ReduceLROnPlateau	–	0.9434
256	Horizontal	OneCycleLR	–	0.9417
256	Horizontal	ReduceLROnPlateau	–	0.9409
256	Horizontal	ReduceLROnPlateau	✓	0.9412
256	Vertical	ReduceLROnPlateau	✓	0.9427
256	Vertical	OneCycleLR	✓	0.9465

Table 10. E-PCN hyperparameter ablation study. Top: batch size and aggregation comparison (no scheduler/BN). Middle: learning rate scheduler comparison at batch=256. Bottom: batch normalization impact. Dashes indicate default settings (no scheduler, no BN). Best: 94.65% with batch=256, vertical aggregation, OneCycleLR, and BN.

several findings. First, smaller batch sizes outperform larger ones, with batch size 256 achieving the best results across all configurations. This suggests that more frequent gradient updates benefit the model’s convergence. Second, the vertical aggregation strategy, which preserves the distinct nature of each graph type through separate channels, outperforms horizontal concatenation. This indicates that maintaining structural separation of the four edge-weight representations (Δ , k_T , z , m^2) provides richer information for classification. The inclusion of adaptive learning rate scheduling improves performance, with OneCycleLR slightly outperforming ReduceLROnPlateau when combined with batch normalization. Finally, batch normalization provides a boost in accuracy, with the best performance of 94.65% achieved using the combination of vertical aggregation, OneCycleLR scheduling, and batch normalization at batch size 256. These results show that careful hyperparameter selection can lead to improvements in model accuracy over the baseline configuration.

6 Discussion

The multi-branch architecture of E-PCN demonstrates that explicit encoding of jet splitting kinematics improves jet classification beyond single-graph models. By constructing four parallel graph representations, each weighted by a kinematic variable (Δ , k_T , z , m^2), and processing them through independently parameterized feature extractors (alternating Chebyshev and edge convolutions), the network learns specialized representations via 1D convolution for classification. Relative to the PCN* baseline trained on identical data (1M jets, 100K per class), E-PCN improves macro-accuracy from 92.49% to 94.67% (+2.36%), macro-AUC from 92.94% to 96.78% (+4.13%), and macro-AUPR from 65.99% to 82.41% (+24.88%). The AUPR gain is significant for practical analyses, as rare signal searches at the LHC require rejecting Standard Model backgrounds at rates exceeding 1000:1 while maintaining signal efficiency. AUPR gains of 81.53% for $H \rightarrow b\bar{b}$ and 51.54% for $H \rightarrow c\bar{c}$

demonstrate that processing kinematic variables through parallel graph branches successfully separates jets with similar substructure but different parton content.

When compared against state-of-the-art models on the JetClass benchmark, E-PCN achieves the highest classification accuracy (94.67%), surpassing ParT (93.12%) by 1.55 percentage points and outperforming ParticleNet (90.15%), P-CNN (88.47%), and PFN (85.21%). The improvement over PCN* (92.49% \rightarrow 94.67%) demonstrates the multi-graph architecture’s value beyond the baseline Chebyshev convolution framework. In terms of AUC, E-PCN (96.78%) performs comparably to ParT (96.87%), trailing by 0.09 percentage points while maintaining the accuracy advantage. This represents a different design trade-off: ParT achieves higher AUC through learned attention weights that flexibly weight particle relationships, whereas E-PCN prioritizes accuracy by hardcoding Lund plane variables into the graph structure. This inductive bias proves effective for heavy-flavor tagging, where E-PCN’s AUC values of 97.61% and 92.87% for $H \rightarrow b\bar{b}$ and $H \rightarrow c\bar{c}$ exceed ParT’s 95.23% and 90.89%. These results support the hypothesis that physics-motivated kinematic features aid bottom and charm identification more effectively than learned attention alone.

To understand which kinematic variables drive classification decisions, Grad-CAM analysis reveals physically interpretable patterns. Angular separation and transverse momentum collectively drive 76% of classifications, consistent with the Cambridge/Aachen clustering algorithm’s emphasis on soft-collinear scales. Leptonic decays weight Δ heavily (45.05% for $H \rightarrow \ell\nu qq'$, 43.98% for $t \rightarrow b\ell\nu$) because neutrinos carry away momentum without depositing detector energy, creating asymmetric angular structures. Gluon jets emphasize k_T (40.24%) due to soft radiation and transverse momentum fluctuations. Heavy-flavor jets show enhanced m^2 sensitivity (13.64% for $H \rightarrow b\bar{b}$) because bottom quarks have rest mass 4.2 GeV [38], large enough to affect pair invariant mass distributions but small enough that kinematic features remain subdominant.

The ablation studies demonstrate complementarity among kinematic variables while revealing individual contributions. Starting from the 92.49% baseline (16-dimensional particle features only), adding any single kinematic variable provides consistent gains: Δ reaches 93.47% (+0.98%), z achieves 93.45% (+0.96%), while k_T and m^2 yield 93.04% and 93.07%. The similar performance of Δ and z suggests both capture jet opening angle information through different formulations: Δ measures geometric separation directly while z encodes momentum sharing that correlates with angular structure. When combining two features, the gains become non-linear, jumping to 94.46–94.61% rather than averaging single-feature improvements. The strongest pairs are (k_T, m^2) at 94.61% and (Δ, m^2) at 94.58%, indicating mass information provides complementary discriminative power when combined with momentum or angular features. Interestingly, the (z, m^2) pair underperforms at 93.35%, barely exceeding single-feature baselines. This suggests redundancy: both encode mass-energy relationships, with z capturing energy sharing through momentum fractions and m^2 measuring invariant mass directly. Moving to three-feature configurations, performance consistently exceeds 94%, with (Δ, z, m^2) reaching 94.65%, only 0.02% below the full model. The (Δ, k_T, z) combination achieves 94.37%, indicating that excluding mass costs more performance than excluding any other variable. This hierarchy suggests m^2 provides discriminative power not fully captured by angular and momentum features, consistent with its role in heavy-flavor identification where quark rest masses become non-negligible. The four-branch E-PCN achieves 94.67%, a 0.02% gain over the best three-feature configuration, representing the cumulative effect of all kinematic variables. The Conv1D learns to weight representations adaptively rather than equally, explaining why simple concatenation or averaging would underperform. Overall, the ablation confirms that performance scales with the number of kinematic channels: one feature gives approximately 93%, two give approximately 94.5%, three give approximately 94.6%, and four reach 94.67%. This progression validates the multi-graph design philosophy: each kinematic variable contributes information that cannot be reconstructed from others, and encoding jet splitting kinematics through parallel graph

representations provides complementary discriminative power.

Despite these performance gains, the architecture comes with computational costs that limit deployment scenarios. Training requires 11 hours on 1M jets (RTX 2080 Ti), and test inference takes 20 hours for 20M samples. Beyond computational considerations, a more substantive limitation involves domain shift between simulation and experiment. The JetClass dataset uses idealized detector simulation [8]: no measurement uncertainties, no pileup from simultaneous collisions, perfect particle reconstruction [8]. Looking forward, several extensions could strengthen the approach. Incorporating jet substructure observables (N -subjettiness [39], energy correlation functions [40]) as additional graph types might capture non-linear effects beyond pairwise kinematics. Enforcing Lorentz equivariance through geometric deep learning frameworks [41, 42] would guarantee boost invariance rather than relying on data augmentation [43, 44]. Multi-task learning, jointly predicting jet flavor, mass, and substructure [45, 46], could improve feature sharing and reduce overfitting. Model compression techniques [47, 48] would enable deployment in real-time trigger systems [49, 50]. Ultimately, evaluation on experimental data with full detector simulation [51] and systematic uncertainties [52] will determine whether physics-informed architectures like E-PCN generalize beyond simulation artifacts. These developments will establish the practical applicability of physics-informed graph neural networks in collider phenomenology [53, 54].

7 Conclusion

We introduce the Explainable Particle Chebyshev Network (E-PCN), a graph neural network that integrates kinematic variables into jet tagging. By processing four parallel graph representations weighted by angular separation (Δ), transverse momentum (k_T), momentum fraction (z), and invariant mass squared (m^2), E-PCN achieves macro-averaged accuracy of 94.67%, AUC of 96.78%, and AUPR of 82.41% on the JetClass benchmark, showing improvements of 2.37%, 4.13%, and 24.88% over the baseline PCN. Through Gradient-weighted Class Activation Mapping (Grad-CAM), we quantify the importance of each kinematic variable. Angular separation and transverse momentum together account for approximately 76% of the model’s predictive power (40.72% and 35.67%, respectively). This is physically meaningful because these quantities encode the collimation structure and dynamics of particle showers, which are core observables in the Lund plane formalism. Momentum fraction and invariant mass squared contribute the remaining signal, distinguishing differences in particle production mechanisms across jet classes.

E-PCN demonstrates that building neural networks around established kinematic principles improves interpretability without sacrificing performance. Our results confirm that E-PCN learns representations aligned with physical intuition, suggesting the model generalizes beyond training data and should remain robust under changing experimental conditions.

References

- [1] O. Aberle, I. Béjar Alonso, O. Brüning et al., *High-Luminosity Large Hadron Collider (HL-LHC): Technical design report*, vol. 10 of *CERN Yellow Reports: Monographs*, CERN, Geneva (2020), [10.23731/CYRM-2020-0010](https://arxiv.org/abs/10.23731/CYRM-2020-0010), [INSPIRE].
- [2] CERN, “High-Luminosity LHC.” <https://home.cern/science/accelerators/high-luminosity-lhc>, 2018.
- [3] S. Mondal and L. Mastrolorenzo, *Machine learning in high energy physics: a review of heavy-flavor jet tagging at the LHC*, *Eur. Phys. J. ST* **233** (2024) 2657 [arXiv:2404.01071] [INSPIRE].

- [4] K. Albertsson et al., *Machine Learning in High Energy Physics Community White Paper*, *J. Phys. Conf. Ser.* **1085** (2018) 022008 [[arXiv:1807.02876](#)] [[INSPIRE](#)].
- [5] H. Qu and L. Gouskos, *ParticleNet: Jet Tagging via Particle Clouds*, *Phys. Rev. D* **101** (2020) 056019 [[arXiv:1902.08570](#)] [[INSPIRE](#)].
- [6] V. Mikuni and F. Canelli, *Point cloud transformers applied to collider physics*, *Mach. Learn. Sci. Tech.* **2** (2021) 035027 [[arXiv:2102.05073](#)] [[INSPIRE](#)].
- [7] C. Shimmin, *Particle Convolution for High Energy Physics*, (2021), [[arXiv:2107.02908](#)] [[INSPIRE](#)].
- [8] H. Qu, C. Li and S. Qian, *Particle Transformer for Jet Tagging*, in *International Conference on Machine Learning*, vol. 162, PMLR, (2022), pp. 18281–18292 [[arXiv:2202.03772](#)] [[INSPIRE](#)].
- [9] S. Gong, Q. Meng, J. Zhang et al., *An efficient Lorentz equivariant graph neural network for jet tagging*, *JHEP* **07** (2022) 030 [[arXiv:2201.08187](#)] [[INSPIRE](#)].
- [10] J. Guo, J. Li, T. Li et al., *Boosted Higgs boson jet reconstruction via a graph neural network*, *Phys. Rev. D* **103** (2021) 116025 [[arXiv:2010.05464](#)] [[INSPIRE](#)].
- [11] F. Ma, F. Liu and W. Li, *Jet tagging algorithm of graph network with Haar pooling message passing*, *Phys. Rev. D* **108** (2023) 072007 [[arXiv:2210.13869](#)] [[INSPIRE](#)].
- [12] Y. Semlani, M. Relan and K. Ramesh, *PCN: A Deep Learning Approach to Jet Tagging Utilizing Novel Graph Construction Methods and Chebyshev Graph Convolutions*, *JHEP* **07** (2024) 247 [[arXiv:2309.08630](#)] [[INSPIRE](#)].
- [13] M. He, Z. Wei and J.-R. Wen, *Convolutional Neural Networks on Graphs with Chebyshev Approximation, Revisited*, in *International Conference on Neural Information Processing Systems*, (2022), [[arXiv:2202.03580](#)] .
- [14] L. Liao, Z. Hu, Y. Zheng et al., *An improved dynamic Chebyshev graph convolution network for traffic flow prediction with spatial-temporal attention*, *Appl. Intell.* **52** (2022) 16104.
- [15] O. Boyaci, M.R. Narimani, K. Davis et al., *Cyberattack Detection in Large-Scale Smart Grids using Chebyshev Graph Convolutional Networks*, in *International Conference on Electrical and Electronics Engineering (ICEEE)*, (2022), pp. 217–221 [[arXiv:2112.13166](#)] .
- [16] D.K. Hammond, P. Vandergheynst and R. Gribonval, *Wavelets on graphs via spectral graph theory*, *Applied and Computational Harmonic Analysis* **30** (2011) 129 [[arXiv:0912.3848](#)] .
- [17] D.I. Shuman, S.K. Narang, P. Frossard et al., *The emerging field of signal processing on graphs: Extending high-dimensional data analysis to networks and other irregular domains*, *IEEE signal processing magazine* **30** (2013) 83 [[arXiv:1211.0053](#)] .
- [18] D.I. Shuman, P. Vandergheynst and P. Frossard, *Chebyshev Polynomial Approximation for Distributed Signal Processing*, in *International Conference on Distributed Computing in Sensor Systems and Workshops (DCOSS)*, (2011), pp. 1–8 [[arXiv:1105.1891](#)] .
- [19] M. Defferrard, X. Bresson and P. Vandergheynst, *Convolutional neural networks on graphs with fast localized spectral filtering*, in *International Conference on Neural Information Processing Systems*, (2016), [[arXiv:1606.09375](#)] .
- [20] Y. Wang, Y. Sun, Z. Liu et al., *Dynamic Graph CNN for Learning on Point Clouds*, *ACM Trans. Graph.* **38** (2019) [[arXiv:1801.07829](#)] [[INSPIRE](#)].

- [21] S.J. Wetzel, S. Ha, R. Iten et al., *Interpretable machine learning in physics: A review*, *arXiv preprint arXiv:2503.23616* (2025) .
- [22] R.R. Selvaraju, M. Cogswell, A. Das et al., *Grad-CAM: Visual Explanations from Deep Networks via Gradient-Based Localization*, in *IEEE International Conference on Computer Vision (ICCV)*, (2017), pp. 618–626 [[arXiv:1610.02391](#)] .
- [23] L. de Oliveira, M. Kagan, L. Mackey et al., *Jet-images — deep learning edition*, *JHEP* **07** (2016) 069 [[arXiv:1511.05190](#)] [[INSPIRE](#)].
- [24] G. Louppe, K. Cho, C. Becot et al., *QCD-Aware Recursive Neural Networks for Jet Physics*, *JHEP* **01** (2019) 057 [[arXiv:1702.00748](#)] [[INSPIRE](#)].
- [25] CMS collaboration, *Boosted jet identification using particle candidates and deep neural networks*, *CMS-DP-2017-049* (2017) .
- [26] P.T. Komiske, E.M. Metodiev and J. Thaler, *Energy Flow Networks: Deep Sets for Particle Jets*, *JHEP* **01** (2019) 121 [[arXiv:1810.05165](#)] [[INSPIRE](#)].
- [27] E.A. Moreno, O. Cerri, J.M. Duarte et al., *JEDI-net: a jet identification algorithm based on interaction networks*, *Eur. Phys. J. C* **80** (2020) 58 [[arXiv:1908.05318](#)] [[INSPIRE](#)].
- [28] F.A. Dreyer and H. Qu, *Jet tagging in the Lund plane with graph networks*, *JHEP* **03** (2021) 052 [[arXiv:2012.08526](#)] [[INSPIRE](#)].
- [29] A. Bogatskiy, T. Hoffman, D.W. Miller et al., *PELICAN: Permutation Equivariant and Lorentz Invariant or Covariant Aggregator Network for Particle Physics*, in *Machine Learning and the Physical Sciences Workshop at NeurIPS*, (2022), [[arXiv:2211.00454](#)] [[INSPIRE](#)].
- [30] Z. Que et al., *JEDI-linear: Fast and Efficient Graph Neural Networks for Jet Tagging on FPGAs*, [arXiv:2508.15468](#).
- [31] A. Wang, Z. Zhao, S. Katel et al., *Spatially Aware Linear Transformer (SAL-T) for Particle Jet Tagging*, [arXiv:2510.23641](#).
- [32] F.A. Dreyer, G.P. Salam and G. Soyez, *The Lund Jet Plane*, *JHEP* **12** (2018) 064 [[arXiv:1807.04758](#)] [[INSPIRE](#)].
- [33] Y.L. Dokshitzer, G.D. Leder, S. Moretti et al., *Better jet clustering algorithms*, *JHEP* **08** (1997) 001 [[arXiv:hep-ph/9707323](#)] [[INSPIRE](#)].
- [34] M. Wobisch and T. Wengler, *Hadronization corrections to jet cross-sections in deep inelastic scattering*, in *Workshop on Monte Carlo Generators for HERA Physics (Plenary Starting Meeting)*, (1998), pp. 270–279 [[arXiv:hep-ph/9907280](#)] [[INSPIRE](#)].
- [35] S. Mandelstam, *Determination of the pion - nucleon scattering amplitude from dispersion relations and unitarity. General theory*, *Phys. Rev.* **112** (1958) 1344 [[INSPIRE](#)].
- [36] H. Qu, C. Li and S. Qian, *JetClass: A Large-Scale Dataset for Deep Learning in Jet Physics*, June, 2022. 10.5281/zenodo.6619768.
- [37] CMS collaboration, *Boosted jet identification using particle candidates and deep neural networks*, *CMS-DP-2017-049* (2017) .
- [38] PARTICLE DATA GROUP collaboration, *Review of Particle Physics*, *Physical Review D* **110** (2024) 030001.
- [39] J. Thaler and K. Van Tilburg, *Identifying boosted objects with N-subjettiness*, *Journal of High Energy Physics* **2011** (2011) 015 [[arXiv:1011.2268](#)] .

- [40] A.J. Larkoski, G.P. Salam and J. Thaler, *Energy correlation functions for jet substructure*, *Journal of High Energy Physics* **2013** (2013) 108 [[arXiv:1305.0007](#)] .
- [41] A. Bogatskiy, B. Anderson, J.T. Offermann et al., *Lorentz Group Equivariant Neural Network for Particle Physics*, in *Proceedings of the 37th International Conference on Machine Learning*, vol. 119 of *PMLR*, (2020), pp. 992–1002.
- [42] J. Spinner, T. Schiffer and T. Plehn, *Lorentz-Equivariant Geometric Algebra Transformers for High-Energy Physics*, *arXiv preprint* (2024) [[arXiv:2405.14806](#)] .
- [43] R. Corso, *Lorentz-invariant augmentation for high-energy physics machine learning*, Master’s thesis, Politecnico di Torino, 2024.
- [44] S. Chen, E. Dobriban and J.H. Lee, *A group-theoretic framework for data augmentation*, *Journal of Machine Learning Research* **21** (2020) 1.
- [45] D. Zhang and D. Shen, *Multi-Modal Multi-Task Learning for Joint Prediction of Multiple Regression and Classification Variables in Alzheimer’s Disease*, *NeuroImage* **59** (2011) 895.
- [46] J. Bingel and A. Søgaard, *Identifying beneficial task relations for multi-task learning in deep neural networks*, in *Proceedings of the 15th Conference of the European Chapter of the Association for Computational Linguistics*, vol. 2, (2017), pp. 164–169.
- [47] S. Francescato et al., *Model compression and simplification pipelines for fast deep neural network inference in FPGAs in HEP*, *The European Physical Journal C* **81** (2021) 1005.
- [48] M. Wielgosz, M. Mertik, A. Skoczeń et al., *The model of an anomaly detector for HiLumi LHC magnets based on Recurrent Neural Networks and adaptive quantization*, *Neurocomputing* **300** (2018) 121.
- [49] Y. Iiyama et al., *Distance-Weighted Graph Neural Networks on FPGAs for Real-Time Particle Reconstruction in High Energy Physics*, *Frontiers in Big Data* **3** (2021) 598927.
- [50] J. Duarte et al., *Fast Inference of Deep Neural Networks for Real-time Computer Vision in Particle Physics Detectors*, in *Proceedings of the 24th International Conference on Computing in High Energy and Nuclear Physics*, (2019), .
- [51] J. Apostolakis et al., *Detector Simulation Challenges for Future Accelerator Experiments*, *Frontiers in Physics* **10** (2022) 913510.
- [52] W. Verkerke, *Systematic uncertainties and profiling*, .
- [53] S. Thais et al., *Graph Neural Networks in Particle Physics*, *Machine Learning: Science and Technology* **3** (2022) 021001 [[arXiv:2203.12852](#)] .
- [54] O. Atkinson et al., *Learning to Classify LHC Topologies with Graph Neural Networks*, *Journal of High Energy Physics* **2022** (2022) 137.

Data availability

The JetClass dataset used in this study is publicly available through [Zenodo](#), with an accompanying [GitHub](#) repository for easy integration into ML workflows.

Acknowledgments

This research is partially supported by research grants from Independent University, Bangladesh (IUB).

A Computational Resources

All experiments are conducted on high-performance computing infrastructure to ensure efficient training and evaluation. Table 11 summarizes the computational resources and software environment utilized.

Component	Specification
CPU	Intel i9-9900K @ 3.60GHz
GPU	NVIDIA RTX 2080 Ti (12 GB)
Memory	64 GB RAM
Software	Ubuntu 22.04, CUDA 12.4, PyTorch/DGL 2.4.0
Training	7.5 min/epoch, 11 h total (1M data)
Testing	20 h (20M data)

Table 11. Computational setup.

B Pseudocode

Algorithm 1 Base Graph Construction from Jet Data

Input: Jet with n particles, each having 16 features (Table 12)

Output: Base Graph

```
1: for each jet do
2:
3:   Build KD-tree for nearest neighbor search
4:   for each particle  $i$  do
5:     Find  $k = 3$  nearest neighbors
6:     Create edges connecting particle  $i$  to each neighbor
7:   end for
8:
9:   return Base graph  $G$ 
10: end for
```

Algorithm 2 Compute Kinematic Edge Features

```
1: function COMPUTEKINEMATICFEATURES(particle_a, particle_b)
2:    $E_a, \mathbf{p}_a \leftarrow$  particle_a.energy, particle_a.momentum
3:    $E_b, \mathbf{p}_b \leftarrow$  particle_b.energy, particle_b.momentum
4:   // Compute rapidity
5:    $y_a \leftarrow 0.5 \times \ln \left( \frac{E_a + p_{a,z}}{E_a - p_{a,z}} \right)$ 
6:    $y_b \leftarrow 0.5 \times \ln \left( \frac{E_b + p_{b,z}}{E_b - p_{b,z}} \right)$ 
7:   // Azimuthal Angle difference
8:    $\phi_a, \phi_b \leftarrow$  particle_a.azimuthal_angle, particle_b.azimuthal_angle
9:    $\Delta\phi \leftarrow \phi_a - \phi_b$   $\triangleright \Delta\phi \in [-\pi, \pi]$ 
10:  // Angular separation
11:   $\Delta \leftarrow \sqrt{(y_a - y_b)^2 + (\Delta\phi)^2}$ 
12:  // Transverse momentum
13:   $p_{T,a} \leftarrow \sqrt{\text{particle\_a}.p_x^2 + \text{particle\_a}.p_y^2}$ 
14:   $p_{T,b} \leftarrow \sqrt{\text{particle\_b}.p_x^2 + \text{particle\_b}.p_y^2}$ 
15:   $k_T \leftarrow \min(p_{T,a}, p_{T,b}) \times \Delta$ 
16:  // Momentum fraction
17:   $z \leftarrow \frac{\min(p_{T,a}, p_{T,b})}{p_{T,a} + p_{T,b}}$ 
18:  // Invariant mass squared
19:   $m^2 \leftarrow (E_a + E_b)^2 - \|\mathbf{p}_a + \mathbf{p}_b\|^2$ 
20:  // Use logarithms for numerical stability
21:  return  $\ln(\Delta), \ln(k_T), \ln(z), \ln(m^2)$ 
22: end function
```

Algorithm 3 Create Four Weighted Graph Representations

```
1: function CREATEWEIGHTEDGRAPHS(base_graph)
2:   // Compute kinematic features for all edges
3:   for each edge (a, b) in base_graph do
4:      $\ln \Delta, \ln k_T, \ln z, \ln m^2 \leftarrow$  COMPUTEKINEMATICFEATURES(particle_a, particle_b)
5:   end for
6:   // Create four graph copies with different edge weights
7:    $G_\Delta \leftarrow$  CopyGraphStructure(base_graph)
8:    $G_\Delta$ .edge_weights  $\leftarrow \ln \Delta$  for all edges
9:    $G_{k_T} \leftarrow$  CopyGraphStructure(base_graph)
10:   $G_{k_T}$ .edge_weights  $\leftarrow \ln k_T$  for all edges
11:   $G_z \leftarrow$  CopyGraphStructure(base_graph)
12:   $G_z$ .edge_weights  $\leftarrow \ln z$  for all edges
13:   $G_{m^2} \leftarrow$  CopyGraphStructure(base_graph)
14:   $G_{m^2}$ .edge_weights  $\leftarrow \ln m^2$  for all edges
15:  // All graphs share identical node features
16:  return  $G_\Delta, G_{k_T}, G_z, G_{m^2}$ 
17: end function
```

Algorithm 4 GNN Feature Extractor

```
1: function (GNNFeatureExtractorgraph, hidden_dim=64)
2:   Initial layer: 16 input features  $\rightarrow$  64 hidden features
3:   // First Chebyshev block
4:    $\mathbf{h}_{1_{cc}} \leftarrow \text{ChebConv}(\text{graph.node\_features}, K = 16)$   $\triangleright K = 16$ 
5:    $\mathbf{h}_{1_{cc}} \leftarrow \text{BatchNorm}(\mathbf{h}_{1_{cc}})$ 
6:    $\mathbf{h}_{1_{cc}} \leftarrow \text{ReLU}(\mathbf{h}_{1_{cc}})$ 
7:   // First EdgeConv block
8:    $\mathbf{h}_{1_{ec}} \leftarrow \text{EdgeConv}(\mathbf{h}_{1_{cc}})$ 
9:    $\mathbf{h}_{1_{ec}} \leftarrow \text{BatchNorm}(\mathbf{h}_{1_{ec}})$ 
10:   $\mathbf{h}_{1_{ec}} \leftarrow \text{ReLU}(\mathbf{h}_{1_{ec}})$ 
11:  // Second Chebyshev block
12:   $\mathbf{h}_{2_{cc}} \leftarrow \text{ChebConv}(\mathbf{h}_{1_{ec}}, K = 16)$ 
13:   $\mathbf{h}_{2_{cc}} \leftarrow \text{BatchNorm}(\mathbf{h}_{2_{cc}})$ 
14:   $\mathbf{h}_{2_{cc}} \leftarrow \text{ReLU}(\mathbf{h}_{2_{cc}})$ 
15:  // Second EdgeConv block
16:   $\mathbf{h}_{2_{ec}} \leftarrow \text{EdgeConv}(\mathbf{h}_{2_{cc}})$ 
17:   $\mathbf{h}_{2_{ec}} \leftarrow \text{BatchNorm}(\mathbf{h}_{2_{ec}})$ 
18:   $\mathbf{h}_{2_{ec}} \leftarrow \text{ReLU}(\mathbf{h}_{2_{ec}})$ 
19:  // Final Chebyshev block
20:   $\mathbf{h}_{f_{cc}} \leftarrow \text{ChebConv}(\mathbf{h}_{2_{ec}}, K = 16)$ 
21:   $\mathbf{h}_{f_{cc}} \leftarrow \text{BatchNorm}(\mathbf{h}_{f_{cc}})$ 
22:   $\mathbf{h}_{f_{cc}} \leftarrow \text{ReLU}(\mathbf{h}_{f_{cc}})$ 
23:  // Aggregate particle features into jet representation
24:  jet_embedding  $\leftarrow \text{MeanPool}(\mathbf{h}_{f_{cc}})$   $\triangleright$  Average across particles  $\rightarrow$  64-dim vector
25:  return jet_embedding
26: end function
```

Algorithm 5 Classifier Network

```
1: function CLASSIFIER(stacked_jet_embeddings)
2:   Input shape: (batch_size, number_of_graph_types, embedding_dimension)
3:   // number of graph types = 4, embedding dimension = 64
4:   // Apply 1x1 convolution across 4 graph channels
5:    $\mathbf{x}_{emb} \leftarrow \text{Conv1D}(\text{stacked\_embeddings}, \text{kernel\_size}=1)$   $\triangleright$  (batch_size, 4, 64)
6:    $\mathbf{x}_{emb} \leftarrow \text{BatchNorm}(\mathbf{x}_{emb})$ 
7:    $\mathbf{x}_{emb} \leftarrow \text{ReLU}(\mathbf{x}_{emb})$ 
8:   // Flatten to single vector
9:    $\mathbf{x}_F \leftarrow \text{Flatten}(\mathbf{x}_{emb})$   $\triangleright$  (batch_size, 256)
10:  // Final classification layers
11:   $\mathbf{x}_{out} \leftarrow \text{Linear}(\mathbf{x}_F, 64)$ 
12:   $\mathbf{x}_{out} \leftarrow \text{BatchNorm}(\mathbf{x}_{out})$ 
13:   $\mathbf{x}_{out} \leftarrow \text{ReLU}(\mathbf{x}_{out})$ 
14:   $\mathbf{x}_{out} \leftarrow \text{Dropout}(\mathbf{x}_{out}, p = 0.1)$ 
15:  logits  $\leftarrow \text{Linear}(\mathbf{x}_{out}, \text{num\_classes}=10)$ 
16:  return logits
17: end function
```

Algorithm 6 GradCAM: Compute Graph Type Importance

```
1: function COMPUTEGRAPHIMPORTANCE(jet_graphs, true_label)
2:   jet_graphs = ( $G_\Delta, G_{k_T}, G_z, G_{m^2}$ ) for a single jet
3:   // Step 1: Get embeddings with gradient tracking enabled
4:   EnableGradients()
5:   emb_Δ ← model_Δ( $G_\Delta$ )
6:   emb_ $k_T$  ← model_ $k_T$ ( $G_{k_T}$ )
7:   emb_ $z$  ← model_ $z$ ( $G_z$ )
8:   emb_ $m^2$  ← model_ $m^2$ ( $G_{m^2}$ )
9:   // Explicitly mark embeddings to retain gradients
10:  emb_Δ.requires_grad ← True; emb_Δ.retain_grad()
11:  emb_ $k_T$ .requires_grad ← True; emb_ $k_T$ .retain_grad()
12:  emb_ $z$ .requires_grad ← True; emb_ $z$ .retain_grad()
13:  emb_ $m^2$ .requires_grad ← True; emb_ $m^2$ .retain_grad()
14:  // Step 2: Forward pass to get prediction
15:  stacked ← Stack([emb_Δ, emb_ $k_T$ , emb_ $z$ , emb_ $m^2$ ], dim=1)
16:  logits ← classifier(stacked)
17:  // Step 3: Extract score for target class
18:  if true_label is provided then
19:    target_class ← true_label
20:  else
21:    target_class ← ArgMax(logits) ▷ Use predicted class
22:  end if
23:  score ← logits[target_class]
24:  // Step 4: Backpropagate to compute gradients
25:  score.backward()
26:  // Step 5: Compute importance as gradient × activation
27:  importance_Δ ← Mean(|emb_Δ.grad| × |emb_Δ|)
28:  importance_ $k_T$  ← Mean(|emb_ $k_T$ .grad| × |emb_ $k_T$ |)
29:  importance_ $z$  ← Mean(|emb_ $z$ .grad| × |emb_ $z$ |)
30:  importance_ $m^2$  ← Mean(|emb_ $m^2$ .grad| × |emb_ $m^2$ |)
31:  // Step 6: Normalize to percentages
32:  total ← importance_Δ + importance_ $k_T$  + importance_ $z$  + importance_ $m^2$ 
33:  percentage_Δ ← (importance_Δ / total) × 100
34:  percentage_ $k_T$  ← (importance_ $k_T$  / total) × 100
35:  percentage_ $z$  ← (importance_ $z$  / total) × 100
36:  percentage_ $m^2$  ← (importance_ $m^2$  / total) × 100
37:  return [percentage_Δ, percentage_ $k_T$ , percentage_ $z$ , percentage_ $m^2$ ]
38: end function
```

C Feature name and Description

Feature	Description
part_px	Particle's momentum in the x-direction
part_py	Particle's momentum in the y-direction
part_pz	Particle's momentum in the z-direction
part_energy	Particle's total energy
part_deta	Difference in pseudorapidity ($\Delta\eta$) with respect to the jet axis or reference
part_dphi	Difference in azimuthal angle ($\Delta\phi$) with respect to the jet axis or reference
part_d0val	Transverse impact parameter d_0 (track displacement measure)
part_d0err	Uncertainty/error on d_0
part_dzval	Longitudinal impact parameter d_z (track displacement in the z-direction)
part_dzerr	Uncertainty/error on d_z
part_charge	Particle charge
part_isChargedHadron	Boolean (0 or 1) indicating if the particle is a charged hadron
part_isNeutralHadron	Boolean indicating if the particle is a neutral hadron
part_isPhoton	Boolean indicating if the particle is a photon
part_isElectron	Boolean indicating if the particle is an electron
part_isMuon	Boolean indicating if the particle is a muon
Derived Feature	
p_T	Transverse momentum, computed as $p_T = \sqrt{\text{part_px}^2 + \text{part_py}^2}$

Table 12. Input features for particle-level jet classification. The dataset contains 16 features per particle: 15 original features read from ROOT files via uproot and 1 derived feature (p_T). Features include kinematic variables (momentum components, energy), angular separations ($\Delta\eta$, $\Delta\phi$), track displacement parameters (d_0 , d_z) with associated uncertainties, and particle identification flags (charged/neutral hadrons, photon, electron, muon).